

High-Resolution Spectroscopy of Raman-scattered He II Lines in the Symbiotic Nova RR Telescopii

Jaejin Shin,¹ Seok-Jun Chang,² *† Hee-Won Lee,¹ Sam Kim,³

¹ Department of Physics and Astronomy, Sejong University, Seoul, Republic of Korea

² Max-Planck-Institut für Astrophysik, Karl-Schwarzschild-Straße 1, 85748 Garching b. München, Germany

³ ESO, Alonso de Córdova 3107, Vitacura, Chile

Accepted XXX. Received YYY; in original form ZZZ

ABSTRACT

Raman-scattered emission features in symbiotic stars provide a powerful diagnostic of mass-loss and transfer processes, as they uniquely probe both ionized and neutral regions within interacting binaries. When resolved with high-resolution spectroscopy, these features encode detailed information on the physical properties of the neutral hydrogen medium. In this work, we present high-resolution spectroscopic observations of the symbiotic nova RR Telescopii obtained with FEROS in 2004 and GHOST in 2024, providing a ~ 20 yr baseline. We report the clear detection of all three Raman-scattered He II lines at 6545 Å, 4851 Å, and 4332 Å, and constrain the distribution and kinematics of H I through line profile analysis. The three Raman lines exhibit distinct relative velocities, indicating that they trace different depths within the H I region. The Raman conversion efficiencies of the three Raman He II lines in 2024 are significantly lower than those in 2004, indicating substantial changes in the physical properties of the neutral hydrogen region. In addition, radiative transfer modeling implies a larger covering factor (opening angle) of the neutral region in 2004 than in 2024. These results indicate that the neutral hydrogen region cannot be characterized by a single H I column density, emphasizing the need for advanced radiative transfer modeling that accounts for the complex kinematics and geometry of the H I region. Overall, these results establish Raman-scattered He II lines as a powerful tool for spectroscopic tomography, allowing for direct constraints on the structure and kinematics of neutral hydrogen in symbiotic binaries.

Key words: stars: symbiotic – stars: RR Tel – stars: novae – radiative transfer – scattering

1 INTRODUCTION

Symbiotic stars are interacting binary stellar systems consisting of a white dwarf (WD) and a red giant (RG). These systems display a range of astrophysical phenomena, including outbursts, prominent ultraviolet (UV) and optical emission lines, collimated outflows, and X-ray emission (Mikołajewska 2012; Munari 2019; Merc 2025). These features result from accretion through the gravitational capture of the slow stellar wind emanating from the giant companion. Consequently, symbiotic stars serve as natural laboratories for studying mass transfer, accretion physics, and binary evolution during the late stages of stellar life (e.g., Kenyon 1986; de Val-Borro et al. 2017; Skopal 2023).

Based on their infrared (IR) spectral energy distributions, symbiotic stars are classified into two types: S-type and D-type. D-type symbiotic stars exhibit an IR excess, indicative of warm dust, whereas S-type systems do not show such an excess (Ivson et al. 1995; Angeloni et al. 2010; Jurkic & Kotnik-Karuzza 2012; Akras et al. 2019). The orbital parameters of D-type binaries are generally poorly constrained (Belczyński et al. 2000; Akras et al. 2019), in contrast to those of S-type systems, which typically have orbital periods of several hundred days (e.g., Mikołajewska 2012). Notably, the mass donor

in D-type symbiotic stars is usually a Mira-type variable or an OH/IR source (e.g., Cho & Kim 2010).

A key observational signature of about half of symbiotic stars is the presence of broad emission features resulting from Raman-scattering (Akras et al. 2019; Merc et al. 2019a,b), which directly probes the neutral hydrogen surrounding the binary system. Early work by Schmid (1989) identified two prominent broad features at 6830 and 7088 Å, produced by Raman-scattering of the O VI resonance doublet at $\lambda\lambda 1032, 1038$ by atomic hydrogen. Subsequent studies revealed additional, weaker Raman-scattered lines of He II with far-UV transitions at $\lambda\lambda 1025, 972$, and 949 being scattered into optical features at 6545, 4851, and 4332 Å (van Groningen 1993; Lee 2012).

These Raman-scattered emission lines provide a direct probe of atomic hydrogen during the mass loss and transfer processes in symbiotic stars. In particular, Raman-scattered He II lines are especially useful because higher-level Raman-scattered He II lines have smaller cross sections, enabling the probing of neutral regions with higher column densities. Intriguingly, Raman-scattered He II emission lines have thus far been detected only in D-type symbiotic stars (i.e., RR Tel, V1016 Cyg, and HM Sge; van Groningen 1993; Lee et al. 2001, 2003; Birriel 2004; Lee 2012). Among these, RR Telescopii (RR Tel) is of particular interest. RR Tel is a well-known symbiotic nova that underwent a nova-like outburst in 1944 and has been fading ever since (e.g., Mayall 1949). According to the American Association

* Corresponding author

† Email: sjchang@mpa-garching.mpg.de

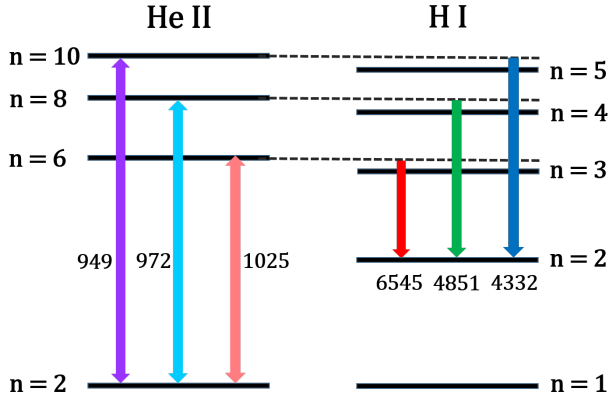


Figure 1. Schematic illustration of He II atomic transitions and the formation of Raman-scattered He II lines near $H\alpha$, $H\beta$, and $H\gamma$. Far-UV He II Balmer lines near the hydrogen Lyman series can excite the ground-state electron, and subsequent de-excitation to the $n = 2$ state emits Raman-scattered He II lines blueward of the hydrogen Balmer lines.

Table 1. Scattering cross sections and wavelengths of three far UV He II Balmer lines for Rayleigh scattering into $n = 1$ ($\sigma_{n=1, \text{Ray}}$) and Raman-scattering into $n = 2$ ($\sigma_{n=2, \text{Ram}}$)

Transition	$6 \rightarrow 2$	$8 \rightarrow 2$	$10 \rightarrow 2$
He II λ (Å)	1025.28	972.13	949.32
$\sigma_{n=2, \text{Ram}}$ (cm ²)	1.2×10^{-21}	1.4×10^{-22}	2.9×10^{-23}
$\sigma_{n=1, \text{Ray}}$ (cm ²)	6.2×10^{-21}	8.3×10^{-22}	1.9×10^{-22}
Raman He II λ (Å)	6544.70	4851.30	4331.74

of Variable Star Observers (AAVSO), RR Tel was observed to be ~ 6 mag in 1948 and steadily dimmed to ~ 12 mag by 2024. Characterized by a Mira-type giant as its mass donor, RR Tel exhibits a pronounced infrared excess consistent with its classification as a D-type symbiotic star. It also displays a remarkably rich spectrum of emission lines spanning a wide range of ionization and excitation states (Selvelli & Bonifacio 2000).

In addition, RR Tel is an excellent object for investigating Raman-scattered He II. Notably, RR Tel exhibits Raman-scattered He II at 6545, 4851, and even 4332 Å (van Groningen 1993; Lee et al. 2001). Because these scattered spectral features probe different parts of the neutral region near the giant star, they provide crucial information about the mass-loss process during the late stages of stellar evolution. However, no quantitative investigation of these scattered features has been carried out. Therefore, a detailed study of Raman-scattered He II is necessary to better understand the nature and physics of the neutral region in symbiotic stars.

For this purpose, we investigate Raman-scattered He II in RR Tel using high-resolution spectroscopic data obtained with Gemini/GHOST and MPG/FEROS. In Section 2, basic atomic physics is summarized. Section 3 describes the observations and data preparation, followed by data analysis in Section 4. The main results, with their theoretical interpretation, are presented in Section 5. Finally, the discussion and summary are provided in Sections 6 and 7.

2 BASIC ATOMIC PHYSICS

Far-UV He II Balmer lines associated with the $2n \rightarrow 2$ transitions have slightly higher energies than the hydrogen Lyman se-

ries ($n \rightarrow 1$). These He II Balmer lines can excite an electron in the ground state of the atomic hydrogen to $n > 2$ states. When the excited electron de-excites to an intermediate state ($n \geq 2$), the inelastic scattering process is referred to as Raman scattering. In contrast, elastic scattering to the ground state is known as Rayleigh scattering. Therefore, He II Balmer lines are efficiently Raman-scattered with atomic hydrogen, generating optical emission features that appear near the hydrogen Balmer lines (e.g., Nussbaumer et al. 1989; van Groningen 1993; Lee et al. 2001). Figure 1 shows a schematic diagram of the first three transitions ($n = 3, 4, 5$), which produce Raman-scattered He II features located blueward of $H\alpha$, $H\beta$, and $H\gamma$.

The interaction between photons and bound electrons is treated using second-order time-dependent perturbation theory, as outlined in standard quantum mechanics references (e.g., Bethe & Salpeter 1957; Sakurai 1967). In particular, the cross sections for Rayleigh and Raman scattering of far-UV photons by neutral hydrogen are described by the Kramers–Heisenberg formula. Table 1 summarizes the cross sections and central wavelengths of the He II Balmer lines, along with the corresponding Raman-scattered features blueward of the hydrogen Balmer lines for $n = 3, 4, 5$ (e.g., Lee 2012; Chang et al. 2023; Kokubo 2024). Note that the wavelengths of far-UV He II and optical Raman He II are expressed in vacuum and air, respectively.

By energy conservation, the wavelength λ_{Raman} of a Raman-scattered line is connected to the incident photon wavelength, λ_{inc} , by

$$\lambda_{\text{inc}}^{-1} = \lambda_{\text{Ram}}^{-1} + \lambda_{\text{Ly}\alpha}^{-1}, \quad (1)$$

where $\lambda_{\text{Ly}\alpha}$ denotes the hydrogen Ly α wavelength. From Equation (1), we obtain

$$\frac{\Delta\lambda_{\text{inc}}}{\lambda_{\text{inc}}} = \left(\frac{\lambda_{\text{inc}}}{\lambda_{\text{Ram}}} \right) \frac{\Delta\lambda_{\text{Ram}}}{\lambda_{\text{Ram}}}. \quad (2)$$

Thus, the inelastic nature of Raman-scattering broadens spectral features by a factor of $\lambda_{\text{Raman}}/\lambda_{\text{inc}}$. These Raman-scattered He II features appear as weak, broadened components near hydrogen Balmer lines.

3 OBSERVATION AND DATA

We performed a high-resolution, deep spectroscopic analysis to investigate Raman-scattered He II in RR Tel based on data obtained with the Gemini High-resolution Optical Spectrograph (GHOST) and the Fiber-fed Extended Range Optical Spectrograph (FEROS). These datasets provide a nearly 20-year baseline for RR Tel.

3.1 Spectroscopy with GHOST

The GHOST observations were carried out on March 25, 2024 (Program ID: GS-2024A-Q-305; PI: Hee-Won Lee). GHOST covers the wavelength range from 3,830 to 10,000 Å with a spectral resolution of $R \sim 56,000$. The observation was conducted in the “standard-resolution” mode. Because Raman-scattered He II features are very faint (e.g., the line flux of Raman-scattered He II at 6545 Å is approximately 1/2000 that of $H\alpha$, see Lim et al. 2025), 2×2 binning was employed to maximize the signal-to-noise ratio in the continuum. With this binning, the effective spectral resolution achieved was approximately $R \sim 40,000$.

To cover both strong (e.g., $H\alpha$) and weak (e.g., Raman-scattered He II) spectral lines, we obtained spectra of RR Tel with various exposure times: 10, 100, 500, and 1,000 seconds. The shorter exposures (10 and 100 seconds) targeted strong emission lines, such as

[O III] and $H\alpha$, while the longer exposures (500 and 1,000 seconds) were designed to detect the Raman-scattered He II line. We note that $H\alpha$ was saturated in these longer exposures. The total on-source exposure time was 3,230 seconds.

We retrieved reduced data from the Gemini archive (Placco et al. 2024) and combined the spectra. Since the $H\alpha$ line was saturated in the longer exposures, we combined only the short exposures for the $H\alpha$ window.

3.2 Spectroscopy with FEROS

To complement our recent GHOST data and establish a long-term baseline, we analyzed archival high-resolution spectra obtained with FEROS. FEROS is a highly efficient echelle spectrograph mounted on the MPG 2.2m telescope located at La Silla Observatory. The instrument provides a spectral resolution of $R \sim 48,000$ and covers 3,500–9,200 Å.

The specific FEROS data utilized were retrieved from the ESO Science Archive (Program ID: 073.D-0724, PI: R. Zamanov). The observations were performed on two separate dates: June 4 and August 30, 2004, thereby providing a ~ 20 -year baseline relative to our GHOST data. For the analysis, four individual exposures, each with a 600 s integration time, were co-added to maximize the signal-to-noise ratio. Since FEROS spectra are not flux-calibrated, we used these data to measure flux ratios between the Raman-scattered He II features and their nearby intrinsic He II emission lines. This ensures that our analysis is largely unaffected by the lack of absolute flux calibration.

4 ANALYSIS

4.1 Line Fitting Procedure

In this work, we performed a multi-component line-fitting analysis of the GHOST and FEROS spectra for RR Tel. Given the large number of emission lines present throughout the spectrum, we conducted separate fitting procedures for $H\alpha$, $H\beta$, and $H\gamma$ windows to minimize interference from unrelated emission or absorption features.

First, for each spectral window ($H\alpha$, $H\beta$, and $H\gamma$), we fitted and subtracted a local continuum determined from the emission-free regions on either side of the lines of interest. We then fitted the emission lines in the residual spectrum, including the Balmer lines, He II, prominent forbidden lines (e.g., [O III], [N II]), and the Raman-scattered He II lines.

During the fitting process, we adopted a Gaussian profile for all emission lines except the Balmer lines. For the Balmer lines, we identified prominent wing features, previously reported in symbiotic stars (Nussbaumer et al. 1989; Lee & Hyung 2000; Chang et al. 2018). Because of these wing features and their asymmetric line profiles, we applied a double Voigt profile to reproduce the observations. Additionally, several constraints were imposed during the fitting process. First, we tied the kinematics of [N II] λ 6548 and [N II] λ 6583, fixing their flux ratio at 1:3, which corresponds to the theoretical branching ratio of this forbidden doublet. Second, we constrained the velocity dispersion ratio between Raman-scattered He II and He II lines to account for the line broadening of Raman-scattered He II emission (see Sect. 2 of Lim et al. 2025). For Raman-scattered He II at 6545, 4851, and 4332 Å, the broadening factors are 6.38 (6544.70/1025.28), 4.99 (4851.30/972.13), and 4.56 (4331.74/949.32), respectively.

We show the fitting results of the GHOST and FEROS data in Figure 2 and Figure 3, respectively. In both figures, strong Balmer

Table 2. Fitting Results of Raman scattered He II and optical He II lines using GHOST and FEROS data. The columns, from left to right, represent line types, line fluxes, central wavelengths, and line widths of He II and Raman-scattered He II.

GHOST			
Lines	Flux (10^{-14} erg s $^{-1}$ cm $^{-2}$)	Center (Å)	σ (Å)
HeII6560	120.06	6559.46	0.39
Raman 6545	10.49	6546.27	2.47
HeII4859	39.07	4858.84	0.38
Raman 4851	1.91	4851.14	1.87
HeII 4338	18.03	4338.23	0.32
Raman 4332	0.95	4332.61	1.47
FEROS			
Lines	Flux (arbitrary units)	Center (Å)	σ (Å)
He II λ 6560	19.31	6559.63	0.49
Raman He II λ 6545	2.14	6545.80	3.10
He II λ 4859	2.70	4859.00	0.40
Raman He II λ 4851	0.20	4851.10	2.00
He II λ 4338	1.23	4338.35	0.39
Raman He II λ 4332	0.09	4332.36	1.79

lines and He II lines are readily apparent in the upper panels. The middle panels show spectra magnified by about a factor of 10, clearly displaying subordinate optical He II lines such as He II λ 6560. The lower panels, magnified by several hundred times, reveal weaker emission lines, including Raman-scattered features. As shown in the lower panels, Raman-scattered He II lines at 6545, 4851, and 4332 Å are clearly detected and fitted with Gaussian profiles.

The best-fit model parameters for the emission lines, including the Raman-scattered features, are listed in Table 2.

4.2 Relative Velocities

From the line-fitting analysis, we measured the line-center positions and fluxes of the Raman-scattered features and the nearby He II emission lines. The line center positions provide kinematic information about the H I region relative to the He II emission region (Choi et al. 2020; Chang et al. 2023). The relative wavelength shift $\Delta\lambda_{c,A}$ and relative velocity $\Delta V_{c,A}$ between the H I medium and He II emission region are defined as follows:

$$\Delta\lambda_{c,A} = (\lambda_A^{\text{atom}} - \lambda_{RA}^{\text{atom}}) - (\lambda_A^{\text{obs}} - \lambda_{RA}^{\text{obs}}), \quad (3)$$

$$\frac{\Delta V_{c,A}}{c} = \left(\frac{\lambda_{A'}^{\text{atom}}}{\lambda_{RA}^{\text{atom}}} \right) \frac{(\lambda_A^{\text{atom}} - \lambda_{RA}^{\text{atom}}) - (\lambda_A^{\text{obs}} - \lambda_{RA}^{\text{obs}})}{\lambda_{RA}^{\text{atom}}}, \quad (4)$$

where λ^{obs} and λ^{atom} denote the observed and atomic line center wavelengths, respectively. Here, the subscript A refers to optical He II emission at 6560.10, 4859.32, and 4338.59 Å, whereas the subscript A' denotes ultraviolet He II emission at 1025.28, 972.13, and 949.32 Å. The subscript RA stands for Raman He II at 6544.70, 4851.30, and 4331.74 Å.

4.3 Raman Conversion Efficiency

As noted earlier, higher-level Raman-scattered He II lines have smaller cross sections. Therefore, the Raman conversion efficiency (RCE) for different Raman-scattered He II lines serves as a diagnostic of the neutral hydrogen region. Since RCE increases with increasing H I column density (N_{HI}) and covering factor of the H I region (Choi

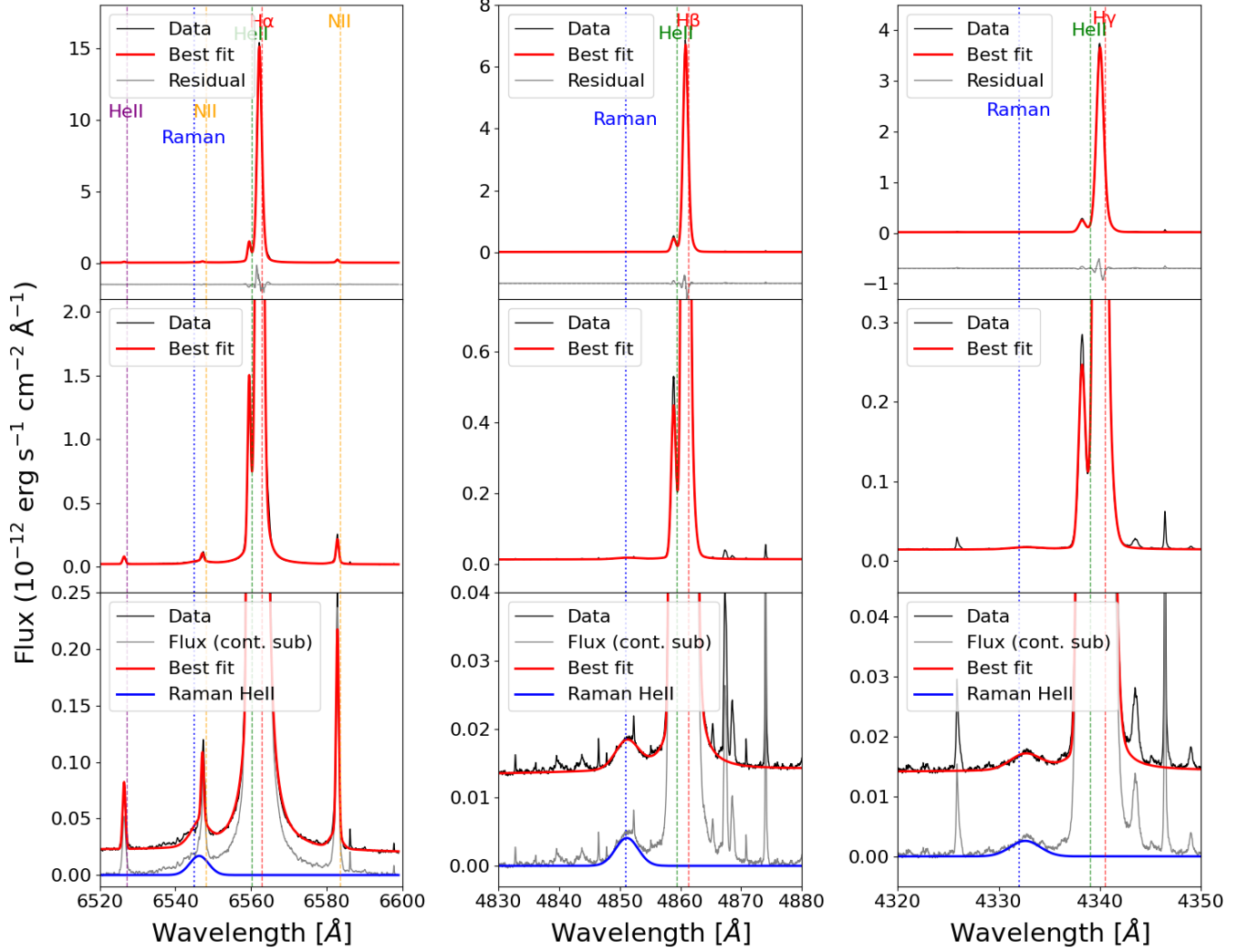


Figure 2. Fitting results of the GHOST data. From left to right, the $H\alpha$, $H\beta$, and $H\gamma$ spectral windows are presented. The top, middle, and bottom panels show the full flux range, a ~ 10 -times magnified view, and a ~ 100 – 200 -times magnified view, respectively. The black, red, and blue lines represent the data, the best-fit model, and the Raman-scattered He II, respectively. The gray lines indicate residuals in the top panel and the continuum-subtracted flux in the bottom panel. The Raman-scattered He II emission lines are clearly visible in the bottom panels.

Table 3. Relative velocities and Raman conversion efficiencies of three Raman-scattered He II lines of GHOST and FEROS spectra. The second and third columns are the relative wavelength shift $\Delta\lambda_{c,A}$ and relative velocity $\Delta V_{c,A}$ between the H I and He II regions, which are defined in Equation (3) and Equation (4), respectively. The fourth column is the Raman conversion efficiency defined in Equation (9).

GHOST			
Raman-scattered He II	$\Delta\lambda_{c,A}$ (Å)	$\Delta V_{c,A}$ (km s ⁻¹)	RCE (%)
$\lambda 6545$	2.21	15.9	10.83
$\lambda 4851$	0.31	3.9	4.74
$\lambda 4332$	1.24	18.8	4.58
FEROS			
Raman-scattered He II	$\Delta\lambda_{c,A}$ (Å)	$\Delta V_{c,A}$ (km s ⁻¹)	RCE (%)
$\lambda 6545$	1.57	11.3	13.74
$\lambda 4851$	0.12	1.5	7.19
$\lambda 4332$	0.86	13.1	6.23

et al. 2020; Lee et al. 2019), it serves as a tracer of the distribution of the scattering region for Raman-scattering (i.e., H I region). If RCEs of multiple Raman-scattered He II lines are observable, their ratio allows us to estimate N_{HI} (Chang et al. 2023; Lim et al. 2025).

The RCE for Raman-scattered He II emission is defined as the photon number ratio between the incident and Raman-scattered radiation. That is,

$$RCE_{\lambda_{\text{Ram}}} = \frac{\Phi_{\lambda_{\text{Ram}}}}{\Phi_{\lambda_{\text{Inc}}}}, \quad (5)$$

where $\Phi_{\lambda_{\text{Ram}}}$ and $\Phi_{\lambda_{\text{Inc}}}$ are the number fluxes of Raman-scattered He II and the corresponding far-UV incident He II. For example, the RCE for Raman-scattered He II $\lambda 6545$ is defined as

$$RCE_{6545} = \frac{\Phi_{6545}}{\Phi_{1025}} \quad (6)$$

where Φ_{1025} and Φ_{6545} denote the total photon fluxes of He II $\lambda 1025$ and Raman-scattered He II $\lambda 6545$, respectively. Similarly, we define RCE_{4851} and RCE_{4332} for Raman-scattered He II $\lambda 4851$ and

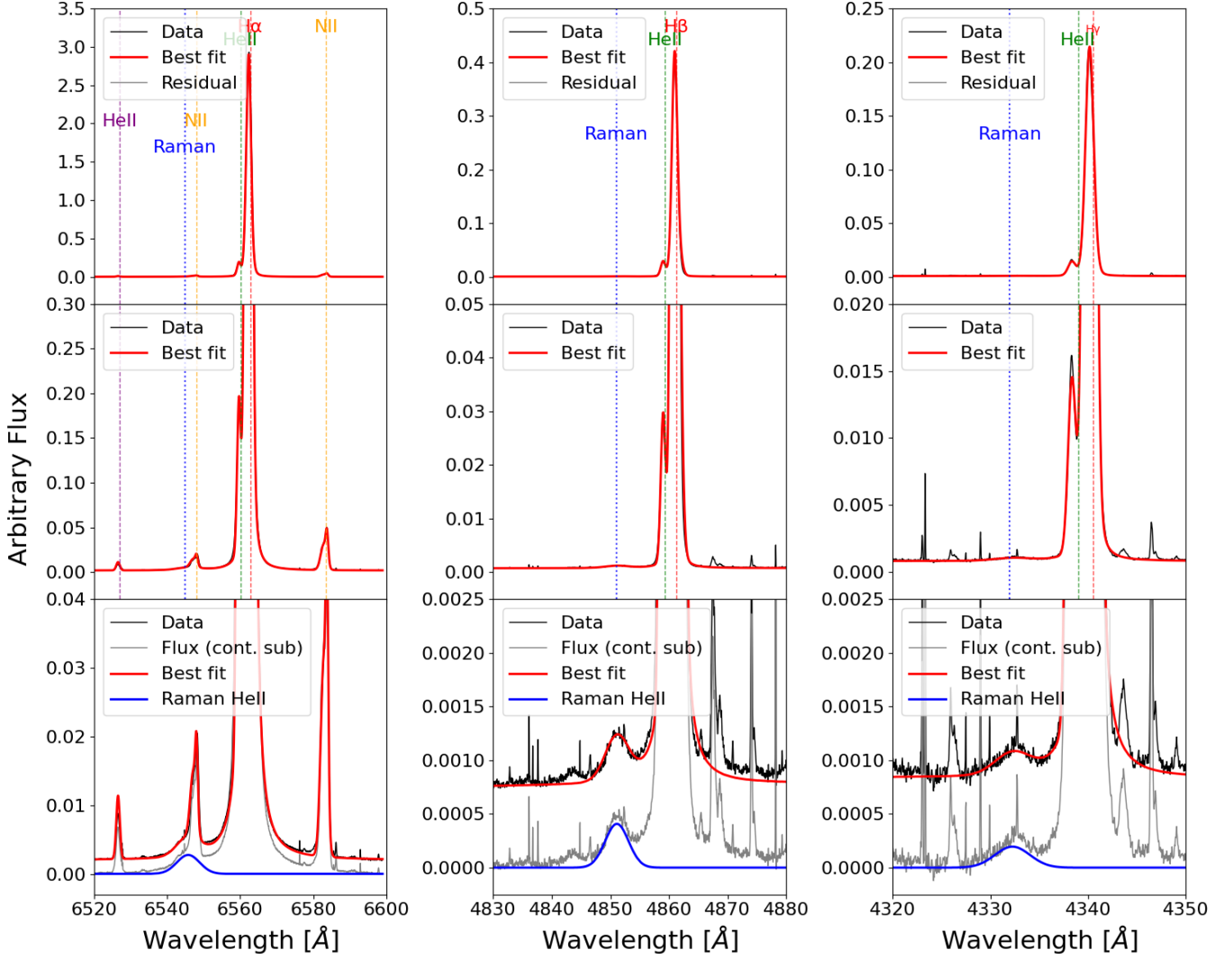


Figure 3. Fitting results of the FEROS data. Other information is the same as in Figure 2.

He II $\lambda 4332$, respectively. The RCE is expected to decrease for higher transitions at the same N_{HI} due to smaller Raman cross sections (see Table 1).

In estimating the RCEs of Raman-scattered He II features, we must infer the number fluxes of the incident He II, as they cannot be directly measured owing to strong interstellar extinction. In particular, the He II $\lambda 1025$ line lies close to the H I Lyman series, where extinction is extremely strong, rendering direct measurements impossible. A practical solution is to employ photoionization modeling, which yields the flux ratio between He II $\lambda 1025$ and an observable optical line such as He II $\lambda 6560$. By combining the observed flux of He II $\lambda 6560$ with the model-predicted ratio, Φ_{1025} can be derived indirectly. Consequently, Equation (6) may be reformulated as

$$RCE_{6545} = \alpha_{6545} \left(\frac{F_{6545}}{F_{6560}} \right), \quad (7)$$

where the coefficient α_{6545} is defined as

$$\alpha_{6545} = \left(\frac{6545}{1025} \right) \left(\frac{F_{6560}}{F_{1025}} \right). \quad (8)$$

In general, we may write

$$RCE_{\lambda_{\text{Ram}}} = \alpha_{\lambda_{\text{Ram}}} \left(\frac{F_{\lambda_{\text{Ram}}}}{F_{\lambda_{\text{Optical}}}} \right), \quad (9)$$

yielding the RCE expressed in observable fluxes once the coefficients $\alpha_{\lambda_{\text{Ram}}}$ are determined.

We employed the publicly available photoionization modeling code CLOUDY (Ferland et al. 2017) to estimate the three coefficients $\alpha_{\lambda_{\text{Ram}}}$. In the same way as in Lim et al. (2025), we assumed a spherical shell geometry to derive the relevant He II fluxes. The nebula was modeled as having a uniform density, photoionized by a blackbody with $T_{\text{eff}} = 2.2 \times 10^5$ K and $L = 1.43 \times 10^4 L_{\odot}$ (Santander-García et al. 2017), from which we found that

$$\alpha_{6545} = 1.24, \quad \alpha_{4851} = 0.97, \quad \alpha_{4332} = 0.87. \quad (10)$$

Table 3 summarizes the relative wavelength shifts $\Delta\lambda_{c,A}$, the relative velocities $\Delta V_{c,A}$ between the H I and He II regions, and the values of the calculated RCEs for the three Raman-scattered He II features obtained with GHOST and FEROS.

Table 4. Estimated H I column densities N_{HI} and opening angles θ_o of the neutral scattering region, derived from the Raman conversion efficiencies of the Raman-scattered He II features at 6545, 4851, and 4332 Å. The listed N_{HI} and θ_o values correspond to those that reproduce the observed RCEs and RCE ratios shown in Figures 4 and 5.

RCE ratio	Data	N_{HI} [cm^{-2}]	θ_o
6545/4851	GHOST	3×10^{21}	50°
	FEROS	4×10^{21}	55°
4851/4332	GHOST	$> 1 \times 10^{23}$	35°
	FEROS	1×10^{23}	50°

5 RESULTS

We analyzed two high-resolution optical spectra of RR Tel obtained roughly 20 years apart.

We aim to obtain information on the changes in the distribution and kinematics of neutral hydrogen from the intensities and line centers of the Raman scattering lines in the two observational datasets. In Section 5.1, we describe and explore the differences in the Raman-scattered He II features between the two spectra based on our line-fitting analysis. In Section 5.2, we constrain the distribution of the H I region by comparing the observed Raman-scattered He II lines with simulations from the 3D Monte Carlo radiative transfer code STaRS (Chang & Lee 2020).

5.1 Observed Properties of the Raman-scattered He II Lines

The relative velocities of the Raman-scattered He II lines, $\Delta V_{c,A}$, quantify the motion of the H I scattering medium with respect to the He II emission region. In Table 3, all three Raman features show positive $\Delta V_{c,A}$ values in both the GHOST and FEROS spectra, indicating that the H I medium, where He II UV photons are Raman-scattered, is outflowing relative to the He II-emitting region.

However, the relative velocities do not follow a monotonic trend across the three Raman transitions. In both spectra, Raman-scattered He II λ 4851 exhibits a $\Delta V_{c,A}$ value that is $\approx 10 \text{ km s}^{-1}$ smaller than that of Raman-scattered He II λ 6545, whereas Raman-scattered He II λ 4332 shows the largest offset. Furthermore, the GHOST data display systematically larger $\Delta V_{c,A}$ values than the FEROS data. These trends imply that the kinematics of the neutral gas are not described by a single outflow speed but instead reflect a more complex velocity structure. We further discuss the non-monotonic behavior of the velocities in Section 6.2.

Table 3 also summarizes the RCEs for the three Raman-scattered He II lines. As expected from their respective Raman cross sections in Table 1, the efficiencies decrease in the sequence RCE_{6545} , RCE_{4851} , and RCE_{4332} for both spectra. However, a significant temporal change is that the RCE values measured from the 2024 GHOST data are approximately 20–35% lower than those from the 2004 FEROS data. Because the RCE depends sensitively on the properties of the neutral region – primarily the H I column density N_{HI} and the effective covering factor – the observed differences likely reflect structural or dynamical changes in the H I envelope over the past two decades, which also depend on the orbital phase. In the next section, we compare the measured RCE values with Monte Carlo radiative transfer simulations to constrain the distribution and evolution of the neutral hydrogen.

5.2 Modeling the H I Distribution with RCEs

To investigate the properties of the H I region, we use the 3D Monte Carlo radiative transfer code STaRS (Chang & Lee 2020). We con-

sider the geometry composed of a central He II point source surrounded by a neutral scattering medium. The neutral region is a pure H I medium characterized by two key parameters: an opening angle θ_o and an H I column density N_{HI} . The central source isotropically emits the far-UV He II emission lines, which can be observed as the Raman-scattered He II lines at 6545, 4851, and 4332 Å through Raman-scattering with atomic hydrogen. Details of the adopted scattering geometry are provided in Appendix A. To cover three Raman-scattered He II lines, we compute models with N_{HI} in the range 10^{20} – 10^{24} cm^{-2} . Figures 4 and 5 present the resulting RCEs and RCE ratios as functions of θ_o and N_{HI} , enabling a direct comparison with the observed values.

In Figure 4, the RCEs increase with N_{HI} when the Raman optical depth, $\tau_{\text{Raman}} = N_{\text{HI}}\sigma_{2s}^{\text{Ram}}$, remains below unity. Once the scattering region becomes optically thick ($\tau_{\text{Raman}} > 1$), the RCE curves flatten because additional increases of N_{HI} no longer enhance the number of Raman-scattered photons; the incident UV photons are already almost fully converted through multiple scatterings within the optically thick medium. Thus, the three Raman-scattered He II lines are most sensitive to the regime in which the corresponding H I layer is optically thin (i.e., $N_{\text{HI}} \lesssim 1/\sigma_{2s}^{\text{Ram}}$). The RCEs also increase monotonically with the opening angle θ_o , since a larger θ_o increases the fraction of incident photons intercepted by neutral gas. Because the covering factor scales as $\theta_o/180^\circ$, dividing one RCE by another removes this geometric dependence. Consequently, the ratios of RCEs for different Raman-scattered He II transitions are independent of θ_o .

In Figure 5, we find that both RCE_{6545}/RCE_{4851} and RCE_{4851}/RCE_{4332} decrease with increasing N_{HI} , and their profiles do not depend on θ_o . In the optically thin regime ($\tau_{\text{Raman}} < 1$) for both lines, the ratios approach the ratios of their Raman-scattering cross sections. In contrast, once both transitions are optically thick ($\tau_{\text{Raman}} > 1$), their RCEs saturate, and the ratios converge to constant values (Lee et al. 2016; Chang et al. 2023). This saturation produces the flat portions of the curves in Figure 5, characteristic of the fully optically thick regime.

Because the RCE ratios are independent of θ_o , they directly constrain N_{HI} of the scattering medium (e.g., Chang et al. 2023; Lim et al. 2025). In the left panel of Figure 5, the observed ratios RCE_{6545}/RCE_{4851} are 2.28 (GHOST) and 1.91 (FEROS), corresponding to $N_{\text{HI}} \approx 3 \times 10^{21} \text{ cm}^{-2}$ (GHOST) and $\approx 4 \times 10^{21} \text{ cm}^{-2}$ (FEROS). In contrast, the right panel shows that the observed ratios RCE_{4851}/RCE_{4332} – 1.03 for GHOST and 1.15 for FEROS – correspond to substantially higher column densities of $N_{\text{HI}} \approx 1 \times 10^{23} \text{ cm}^{-2}$ (FEROS) and a lower limit $N_{\text{HI}} > 1 \times 10^{23} \text{ cm}^{-2}$ (GHOST, whose ratio falls below the values reproduced by the single-zone model). Thus, for both data, N_{HI} inferred from RCE_{6545}/RCE_{4851} are more than an order of magnitude smaller than those inferred from RCE_{4851}/RCE_{4332} . This discrepancy demonstrates that a single value of N_{HI} cannot simultaneously reproduce all three Raman-scattered He II features, implying that the neutral region in RR Tel must have a complex structure. Since our modeling assumes a single-zone H I distribution, it is unable to capture this complexity; we further discuss this limitation in Section 6.2.

In addition to estimating N_{HI} , we also constrain the opening angle θ_o . In the left panel of Figure 4, at the column densities inferred from RCE_{6545}/RCE_{4851} ($N_{\text{HI}} \approx 3 \times 10^{21} \text{ cm}^{-2}$ for GHOST and $4 \times 10^{21} \text{ cm}^{-2}$ for FEROS), $\theta_o \approx 50^\circ$ for GHOST and $\theta_o \approx 55^\circ$ for FEROS. From the center and right panels, adopting the higher N_{HI} from RCE_{4851}/RCE_{4332} yields $\theta_o \approx 35^\circ$ (GHOST) and $\theta_o \approx 50^\circ$ (FEROS). Table 4 summarizes estimated N_{HI} and θ_o values. Overall, the GHOST data suggest narrower opening angles than the

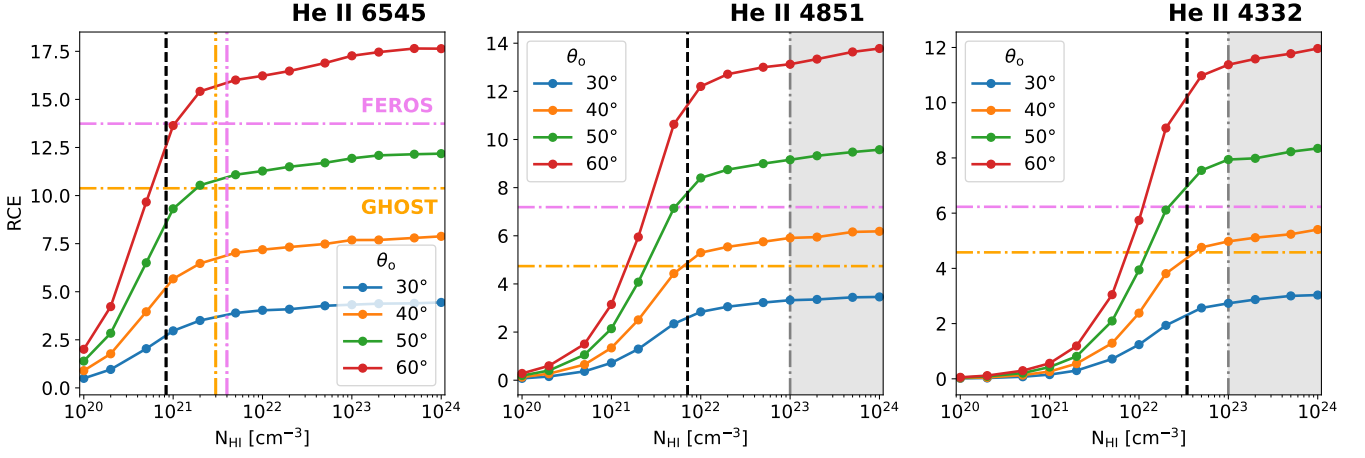


Figure 4. Simulated Raman conversion efficiencies (RCEs) for the Raman-scattered He II λ 6545 (left), 4851 (center), and 4332 (right) features as a function of N_{HI} in the range of 10^{20} – 10^{24} cm^{-2} . Solid curves indicate different opening angles θ_o of the H I region, ranging from 30° to 60° . Horizontal dot-dashed lines denote the observed RCE values from the GHOST (orange) and FEROS (violet) spectra (Table 3). Vertical black dashed lines represent the H I column densities at which the Raman optical depth is unity, $\tau_{\text{Raman}} = N_{\text{HI}} \sigma_{2s}^{\text{Ram}} = 1$, for each line. In the left panel, the vertical orange and violet dot-dashed lines indicate $N_{\text{HI}} \approx 3 \times 10^{21}$ cm^{-2} (GHOST) and 4×10^{21} cm^{-2} (FEROS) estimated from the observed ratio RCE_{6545}/RCE_{4851} in the left panel of Figure 5. In the center and right panels, the gray dot-dashed line marks $N_{\text{HI}} \approx 1 \times 10^{23}$ cm^{-2} from the FEROS ratio RCE_{4851}/RCE_{4332} , and the gray shaded region indicates $N_{\text{HI}} > 10^{23}$ cm^{-2} ; the GHOST ratio falls below the values reproduced by the single-zone model and is therefore shown as a lower limit ($N_{\text{HI}} > 1 \times 10^{23}$ cm^{-2}). The flattening of the RCE profiles to the right of the black dashed lines shows that the RCE becomes insensitive to increasing N_{HI} once the scattering region is optically thick ($\tau_{\text{Raman}} > 1$).

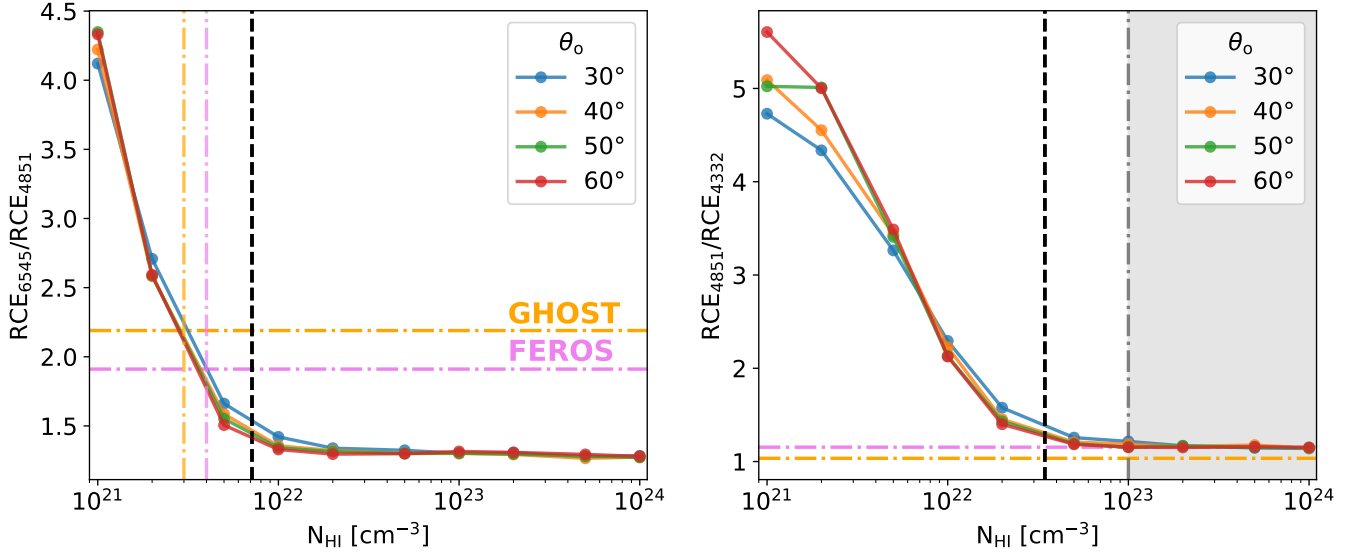


Figure 5. Ratios of the simulated Raman conversion efficiencies, RCE_{6545}/RCE_{4851} (left) and RCE_{4851}/RCE_{4332} (right), as functions of N_{HI} . Horizontal dot-dashed lines represent the observed ratios from the GHOST (orange) and FEROS (violet) spectra as shown in Table 3. Vertical black dashed lines in each panel mark the column density for which $\tau_{\text{Raman}} = 1$ for the corresponding shorter-wavelength Raman-scattered line (He II λ 4851 in the left panel and He II λ 4332 in the right panel). In the left panel, the vertical orange and violet dot-dashed lines denote the N_{HI} values that reproduce the observed RCE_{6545}/RCE_{4851} ratios for the GHOST ($\approx 3 \times 10^{21}$ cm^{-2}) and FEROS ($\approx 4 \times 10^{21}$ cm^{-2}) spectra. In the right panel, the gray dot-dashed line marks the $N_{\text{HI}} \approx 1 \times 10^{23}$ cm^{-2} that reproduces the observed FEROS ratio RCE_{4851}/RCE_{4332} , and the gray shaded region indicates $N_{\text{HI}} > 10^{23}$ cm^{-2} ; the GHOST ratio falls below the values reproduced by the single-zone model and is shown as a lower limit ($N_{\text{HI}} > 1 \times 10^{23}$ cm^{-2}). Other information is the same as in Figure 4.

FEROS data. The implications of these differences – including their connection to the relative velocity shifts of the Raman lines – are discussed in Section 6.1.

In summary, the values of N_{HI} and θ_o inferred from the comparison between observed and simulated RCEs point to a neutral region

whose structure cannot be described by a single-zone geometry. The markedly different N_{HI} required to match the three Raman-scattered He II features implies that each transition probes a distinct depth within the H I envelope, reflecting spatial variations in both density and kinematics. These results highlight the need for a more complex

kinematics and distribution of the H I medium in RR Tel, which we discuss further in the following section.

6 DISCUSSION

We identify significant differences in the RCEs between the GHOST and FEROS datasets, indicating substantial changes in the Raman-scattered He II lines and the physical properties of the neutral hydrogen region. Raman-scattered He II lines in the 2004 FEROS data show higher RCEs and a smaller relative velocity than those in the 2024 GHOST data. Our radiative transfer modeling further indicates a significant change in the physical properties of the neutral hydrogen region between the two datasets. However, the modeling results of each spectrum yield different N_{HI} values, estimated from the ratios RCE_{6545}/RCE_{4851} and RCE_{4851}/RCE_{4332} . This indicates the presence of a complex H I medium structure, because the adopted model assumes a single-zone geometry characterized by a single N_{HI} . In the following, we discuss the physical origins of the differences between the two spectra in 2004 and 2024, and how Raman-scattered He II traces the complex kinematics and distribution of the H I region in RR Tel.

6.1 Physical changes of the H I region in RR Tel

Our principal result is the significant change in the physical properties of the neutral hydrogen region between the FEROS (2004) and GHOST (2024) datasets. We show that the neutral region in 2004 had a larger covering factor (opening angle) than in 2024, as shown in Section 5.2. Several physical mechanisms may account for these changes, including intrinsic variations of the Mira wind and changes in the binary geometry.

One possible explanation lies in variations in Mira’s mass-loss rate, which is closely linked to the extent and density of the surrounding neutral region (e.g., Kotnik-Karuza & Friedjung 2001). In particular, the smaller inferred covering factor in the GHOST data indicates that the neutral hydrogen region was less extended during the GHOST epoch than during the FEROS epoch. When considered together with the larger relative velocities of Raman-scattered He II features in the GHOST data compared to those of the FEROS data (see Table 3), this suggests a change in the kinematic and geometric structure of the Mira wind.

Although no significant photometric variations are evident in the AAVSO monitoring data, it should be noted that the optical magnitude may be dominated primarily by strong ionization lines (e.g., H α and [O III]) rather than by the stellar continuum of the giant star. Therefore, continued spectroscopic and photometric monitoring is required to clarify the detailed mass-loss processes and/or the binary orbital motion of RR Tel (e.g., Jurkic & Kotnik-Karuza 2012).

Another possible explanation is orbital motion. Orbital motion may have caused a substantial change in the covering factor of the neutral region relative to the He II emission region. If the orbit is highly eccentric, the separation between the white dwarf and Mira components could vary significantly, thereby influencing the inferred neutral hydrogen column density and the covering factor, and hence the overall RCE. An observational hint was provided by Schmid & Schild (2002), who conducted spectropolarimetric monitoring of the position angle of polarized Raman-scattered O VI. Over seven years of observations of RR Tel, they measured a mean rotation rate of $1.3^\circ \text{ yr}^{-1}$, corresponding to an orbital period of about 270 years. While the 270-year orbital period lacks corroboration from alternative methods and the orbital elements remain poorly constrained, the

20-year gap between observation periods likely accounts for the significant variation in the resulting RCE. In addition, the fraction of the neutral region illuminated by the UV emission depends on the observer’s line of sight, analogous to variations in the projected area in ellipsoidal variables. However, it is beyond the scope of this paper to quantify the effect of the binary phase.

6.2 Limitations of the single-zone model

The H I column density is one of the crucial parameters to determine properties of Raman-scattered features such as Raman-scattered He II and O VI lines (Schmid & Schild 1994; Skopal et al. 2006; Choi et al. 2020; Heo et al. 2021). For this reason, we consider a geometry for radiative transfer modeling composed of a central source surrounded by a partial spherical region characterized by a single H I column density N_{HI} and opening angle θ_o (i.e., a single-zone H I geometry). As the ratios of RCEs monotonically increase with increasing N_{HI} , we estimate N_{HI} using two RCE ratios, RCE_{6545}/RCE_{4851} and RCE_{4851}/RCE_{4332} .

However, the values of N_{HI} and θ_o inferred from these two ratios are inconsistent (Table 4); the two ratios imply systematically different values of N_{HI} and θ_o . Furthermore, Raman-scattered He II lines exhibit different relative velocities; $\Delta V_{c,A}$ at 4851 Å is $\approx 10 \text{ km s}^{-1}$ smaller than that at 4332 Å. This indicates that the different Raman-scattered He II lines are formed in physically distinct regions of the H I envelope with different kinematics.

The H I distribution is determined by stellar wind from a red giant, as discussed in Section 6.1. Hence, N_{HI} at the emission region near a white dwarf is not isotropic in various lines of sight (Lee & Lee 1997). Furthermore, spectropolarimetric observations of Raman-scattered O VI features by Schmid & Schild (1994) reveal a wavelength-dependent position angle, indicating a complex Raman-scattering behavior in anisotropic H I distribution (e.g., Harries & Howarth 1996). Thus, the neutral scattering region in RR Tel cannot be fully described by a single-zone H I geometry. Instead, the inferred N_{HI} structure points to a stratified or multi-component neutral envelope with spatially varying density and kinematics.

6.3 Raman He II lines as tracers of complex H I gas

As shown in Section 5.2, RCE ratios can be used as indicators of the H I column density. However, their interpretation is limited by the complexity of the H I distribution, as discussed in Section 6.2. One possible systematic uncertainty is the estimation of the incident far-UV He II photon fluxes, which are not directly observable and are instead inferred from the optical He II recombination lines using photoionization modeling. In this work, we adopted a fixed ionizing-source temperature and luminosity to compute the conversion factors $\alpha_{\lambda_{\text{Ram}}}$. These assumptions may affect the ionization structure and the location of the H I ionization front, and therefore can influence the quantitative values of N_{HI} and θ_o inferred from the RCEs.

However, the relative strengths of the He II recombination lines are not expected to vary strongly with the absolute luminosity of the ionizing source, and their dependence on the adopted source temperature is limited once the emitting gas remains in a highly ionized recombination regime (Osterbrock 1989; Lim et al. 2025). Therefore, plausible variations in the ionizing-source parameters may shift the quantitative estimates of N_{HI} and θ_o of H I gas, but are unlikely to by themselves produce the observed line-dependent discrepancies. In particular, they do not explain the distinct relative velocity shifts among the Raman-scattered He II features. This suggests that the inconsistency between the RCE ratios is more naturally interpreted as

evidence that the three Raman lines sample different regions of the neutral layers.

For this reason, we investigate the spatial distribution of locations where He II UV photons undergo Raman scattering (i.e., the last-scattering locations). Most Raman scattering occurs near the ionization front in optically thick H I gas, whereas in the optically thin case, the scattering is more uniformly distributed (see Appendix B for details). Consequently, even for media with the same N_{HI} , photons of each He II UV line are Raman-scattered at different locations due to their different cross sections, giving rise to a stratified spatial distribution of the Raman-scattered He II $\lambda 6545$, 4851 , and 4332 features.

As shown in Table 3, the observed kinematic hierarchy is consistent with the stratified scattering picture inferred from the Monte Carlo simulations. This kinematic difference suggests that the kinematics of the neutral medium are coupled to the distribution of H I. The representative outflow speed of the Mira wind is $10\text{--}20\text{ km s}^{-1}$, implying that the relative velocity of the main wind region is expected to be smaller than that of the launching site by this characteristic range. Indeed, the systematically smaller velocity of Raman He II $\lambda 4851$ compared to He II $\lambda 4332$ is evident in both the FEROS and GHOST spectra. Moreover, the overall relative velocities measured in 2004 are smaller than those in 2024 by $\sim 2\text{--}6\text{ km s}^{-1}$.

The observed differences among the three Raman-scattered He II lines therefore suggest that they do not simply provide redundant measurements of a single H I column density. Instead, each line carries complementary information about a different effective scattering depth and velocity component within the neutral envelope. This makes the Raman He II triplet a potentially powerful diagnostic of the stratified H I wind in RR Tel and other symbiotic stars.

6.4 Dusty neutral region

The IR excess near $3\text{ }\mu\text{m}$ shown in RR Tel indicates the presence of a dust component with a temperature $T \sim 10^3\text{ K}$ (e.g., Angeloni et al. 2010; Jurkic & Kotnik-Karuzza 2012). In understanding the discrepancy between the observations and the theoretical model, an additional factor that warrants consideration is the possible influence of dust within the neutral scattering region.

The scattering cross sections for the far-UV He II lines at 1025 , 972 , and 949 \AA differ substantially, and therefore the formation sites of the corresponding Raman-scattered features are not identical, but instead are stratified according to the local H I column density. For instance, the Raman-scattered He II $\lambda 4332$ feature is expected to arise primarily in the deeper layers of the neutral region, where the column density reaches $N_{\text{HI}} \sim 10^{23}\text{ cm}^{-2}$. In contrast, the Raman-scattered feature at 6545 \AA originates in a relatively shallow layer characterized by a column density more than an order of magnitude lower.

If dust is present and mixed with neutral gas in these regions, extinction will preferentially affect shorter-wavelength photons; in particular, He II $\lambda 949$ photons are much more susceptible to extinction than He II $\lambda 1025$ photons (e.g., Seon & Draine 2016; Lin & Yan 2024). This differential extinction would naturally lead to a selective suppression of the Raman-scattered He II $\lambda 4332$ feature relative to the He II $\lambda 6545$ feature. Consequently, variations in the dust content or its spatial distribution across the neutral region could provide an additional mechanism for the observed differences in RCE among the Raman features, complementing the role of geometry, kinematics, and ionization structure.

6.5 Future modeling and observations

A comprehensive radiative-transfer model is required to fully interpret the information imprinted on Raman-scattered He II lines. The present results show that the RCEs and velocity shifts cannot be explained by a single parameter, such as N_{HI} , or by a simple kinematic prescription alone. Instead, they are affected by several coupled factors, including the geometry and kinematics of the neutral wind, the ionization structure set by the white dwarf radiation field, and possible dust extinction within the neutral region.

Future modeling should therefore combine Raman radiative transfer with a physically motivated H I distribution. This may be achieved by adopting a stellar-wind geometry (Lee & Lee 1997) or by using realistic hydrodynamic simulations (Lee et al. 2022). Realistic photoionization modeling is also required to estimate the He II emissivity and the location of the hydrogen ionization front, since the luminosity and temperature of the white dwarf, as well as the accretion rate, determine the ionization state of the gas in symbiotic stars (Kuuttila & Gilfanov 2021; Kuuttila et al. 2021). In addition, as discussed in Section 6.4, dust in the neutral gas should be included, because differential far-UV extinction can modify the relative strengths of the incident He II lines before Raman scattering occurs.

Such modeling will inevitably involve degeneracies among wind geometry, ionization structure, and dust attenuation. Future high-resolution monitoring of the Raman-scattered He II features, particularly their temporal velocity shifts and profile asymmetries, can help constrain the relative contributions of different regions of the neutral wind. Such observations can also test whether changes in the RCEs are mainly driven by variations in the neutral wind geometry, the ionization structure, or dust attenuation. A simultaneous analysis of the three Raman-scattered He II lines may therefore provide important constraints on the structure and kinematics of the slow stellar wind from the Mira component.

7 CONCLUSION

We have analyzed Raman-scattered He II lines using high-resolution spectra obtained with FEROS in 2004 and GHOST in 2024. By comparing the Raman conversion efficiencies over ~ 20 yr baseline with Monte Carlo radiative transfer modeling, we investigated the structure and evolution of the neutral hydrogen scattering region. Our main conclusions are summarized as follows.

- We detected the Raman-scattered He II lines blueward of $H\alpha$, $H\beta$, and $H\gamma$ in both datasets, and performed line-fitting analysis to derive flux ratios relative to the neighboring optical He II emission lines.
- From these measurements, we derived the Raman conversion efficiencies (RCEs) and found that the RCEs in the 2004 FEROS data are substantially higher than those in the 2024 GHOST data.
- When interpreted with Monte Carlo modeling adopting a simple scattering geometry, these results suggest that the neutral region in 2004 had a larger covering factor (opening angle) than in 2024.
- However, the inconsistency between the RCEs inferred from different Raman He II lines demonstrates that the neutral scattering region cannot be fully described by a single-zone geometry.
- Together with distinct kinematics among the various Raman-scattered He II lines, this indicates that the Raman-scattered He II lines probe a stratified and kinematically complex neutral medium, making them a powerful diagnostic tool for studying the structure and kinematics of the neutral region in symbiotic systems.

Future work will involve radiative transfer modeling with refined

scattering geometries that incorporate the effects of dust and binary orbital phase.

ACKNOWLEDGEMENTS

This work was supported by the National Research Foundation of Korea (NRF) grants funded by the Korea government (No. NRF-2023R1A2C1006984). This work was supported by the K-GMT Science Program (PID: GS-2024A-Q-305) of the Korea Astronomy and Space Science Institute (KASI). Based on observations obtained at the international Gemini Observatory, a program of NSF NOIRLab, which is managed by the Association of Universities for Research in Astronomy (AURA) under a cooperative agreement with the U.S. National Science Foundation on behalf of the Gemini Observatory partnership: the U.S. National Science Foundation (United States), National Research Council (Canada), Agencia Nacional de Investigación y Desarrollo (Chile), Ministerio de Ciencia, Tecnología e Innovación (Argentina), Ministério da Ciência, Tecnologia, Inovações e Comunicações (Brazil), and Korea Astronomy and Space Science Institute (Republic of Korea). We acknowledge with thanks the variable star observations from the *AAVSO* International Database contributed by observers worldwide and used in this research. We used generative AI tools (e.g., ChatGPT, OpenAI, and Claude, Anthropic) for language editing and coding assistance. All AI-generated suggestions were critically reviewed, tested, and validated by the authors, who take full responsibility for the scientific content and results.

DATA AVAILABILITY

The data presented in this work are available through the Gemini Observatory Archive (Program ID: GS-2024A-Q-305; PI: Hee-Won Lee) and the ESO Science Archive (Program ID: 073.D-0724; PI: R. Zamanov). The STaRS code used for radiative transfer simulations is publicly available at <https://github.com/csj607/STaRS>.

REFERENCES

- Akras S., Guzman-Ramirez L., Leal-Ferreira M. L., Ramos-Larios G., 2019, *ApJS*, **240**, 21
- Angeloni R., Contini M., Ciroi S., Rafanelli P., 2010, *MNRAS*, **402**, 2075
- Belczyński K., Mikołajewska J., Munari U., Ivison R. J., Friedjung M., 2000, *A&AS*, **146**, 407
- Bethe H. A., Salpeter E. E., 1957, *Quantum Mechanics of One and Two Electron Atoms*. Berlin: Springer; New York: Academic Press
- Birriel J. J., 2004, *ApJ*, **612**, 1136
- Chang S.-J., Lee H.-W., 2020, *Journal of Korean Astronomical Society*, **53**, 169
- Chang S.-J., Lee H.-W., Lee H.-G., Hwang N., Ahn S.-H., Park B.-G., 2018, *ApJ*, **866**, 129
- Chang S.-J., Lee H.-W., Kim J., Choi Y.-H., 2023, *ApJ*, **949**, 106
- Cho S.-H., Kim J., 2010, *ApJ*, **719**, 126
- Choi B.-E., Chang S.-J., Lee H.-G., Lee H.-W., 2020, *ApJ*, **889**, 2
- Ferland G. J., et al., 2017, *Revista Mexicana de Astronomía y Astrofísica*, **53**, 60
- Harries T. J., Howarth I. D., 1996, *A&AS*, **119**, 61
- Heo J.-E., Lee H.-W., Angeloni R., Palma T., Di Mille F., 2021, *ApJ*, **915**, 105
- Ivison R. J., Seaquist E. R., Schwarz H. E., Hughes D. H., Bode M. F., 1995, *MNRAS*, **273**, 517
- Jurkic T., Kotnik-Karuza D., 2012, *A&A*, **544**, A35
- Kenyon S. J., 1986, *The symbiotic stars*
- Kokubo M., 2024, *MNRAS*, **529**, 2131

- Kotnik-Karuza D., Friedjung M., 2001, *Odessa Astronomical Publications*, **14**, 44
- Kuuttila J., Gilfanov M., 2021, *MNRAS*, **507**, 594
- Kuuttila J., Gilfanov M., Woods T. E., Seitzzahl I. R., Ruiter A. J., 2021, *MNRAS*, **500**, 3763
- Lee H.-W., 2012, *ApJ*, **750**, 127
- Lee H.-W., Hyung S., 2000, *ApJ*, **530**, L49
- Lee H. W., Lee K. W., 1997, *MNRAS*, **287**, 211
- Lee H.-W., Kang Y.-W., Byun Y.-I., 2001, *ApJ*, **551**, L121
- Lee H.-W., Sohn Y.-J., Kang Y. W., Kim H.-I., 2003, *ApJ*, **598**, 553
- Lee Y.-M., Lee D.-S., Chang S.-J., Heo J.-E., Lee H.-W., Hwang N., Park B.-G., Lee H.-G., 2016, *ApJ*, **833**, 75
- Lee Y.-M., Lee H.-W., Lee H.-G., Angeloni R., 2019, *MNRAS*, **487**, 2166
- Lee Y.-M., Kim H., Lee H.-W., 2022, *ApJ*, **931**, 142
- Lim J., Chang S.-J., Shin J., Lee H.-W., Kim J., Kim H.-S., Choi B.-E., Lee H.-G., 2025, *ApJ*, **979**, 124
- Lin Z., Yan R., 2024, *A&A*, **691**, A201
- Mayall M. W., 1949, *Harvard College Observatory Bulletin*, **919**, 15
- Merc J., 2025, *Galaxies*, **13**, 49
- Merc J., Gális R., Wolf M., 2019a, *Research Notes of the American Astronomical Society*, **3**, 28
- Merc J., Gális R., Wolf M., 2019b, *Astronomische Nachrichten*, **340**, 598
- Mikołajewska J., 2012, *Baltic Astronomy*, **21**, 5
- Munari U., 2019, *arXiv e-prints*, p. arXiv:1909.01389
- Nussbaumer H., Schmid H. M., Vogel M., 1989, *A&A*, **211**, L27
- Osterbrock D. E., 1989, *Astrophysics of gaseous nebulae and active galactic nuclei*
- Placco V. M., et al., 2024, *Research Notes of the American Astronomical Society*, **8**, 312
- Sakurai J. J., 1967, *Advanced Quantum Mechanics*. Massachusetts: Addison-Wesley Publishing Company
- Santander-García M., Bujarrabal V., Alcolea J., Castro-Carrizo A., Sánchez Contreras C., Quintana-Lacaci G., Corradi R. L. M., Neri R., 2017, *A&A*, **597**, A27
- Schmid H. M., 1989, *A&A*, **211**, L31
- Schmid H. M., Schild H., 1994, *A&A*, **281**, 145
- Schmid H. M., Schild H., 2002, *A&A*, **395**, 117
- Selvelli P. L., Bonifacio P., 2000, *A&A*, **364**, L1
- Seon K.-I., Draine B. T., 2016, *ApJ*, **833**, 201
- Skopal A., 2023, *AJ*, **165**, 258
- Skopal A., Vittone A. A., Errico L., Otsuka M., Tamura S., Wolf M., Elkin V. G., 2006, *A&A*, **453**, 279
- de Val-Borro M., Karovska M., Sasselov D. D., Stone J. M., 2017, *MNRAS*, **468**, 3408
- van Groningen E., 1993, *MNRAS*, **264**, 975

APPENDIX A: SCATTERING GEOMETRY

In Section 5.2, we use the 3D grid-based radiative transfer code STaRS to compute the Raman conversion efficiency (RCE) of Raman He II lines at 6545, 4851, and 4332 Å, assuming a single zone H I column density. This section describes details of the scattering geometry and simulation.

Figure A1 shows the schematic illustration of the scattering geometry, composed of a central He II emission region and H I partial sphere. The He II emission region is a highly ionized and compact gas near the white dwarf, while the H I region from the red giant is spatially diffused and surrounds the ionized region. As the emission region is much more compact than the H I region, we set the He II emission source at the center of the geometry. Since the neutral gas is coming from the direction of the red giant, we assume a partial spherical H I geometry surrounding the central source in the side of the red giant (+x direction). The H I region is characterized by an inner radius R_i , outer radius R_o , a half opening angle θ_o , and H I column density N_{HI} . As the inner region can be ionized by UV

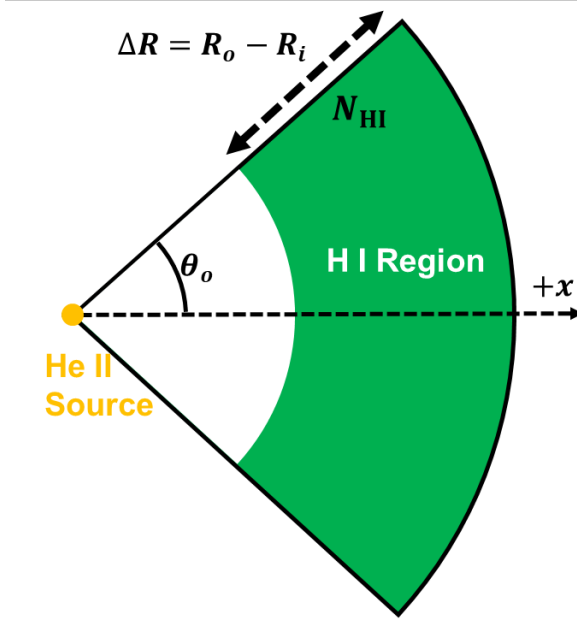


Figure A1. Schematic illustration of the scattering geometry for the radiative transfer modeling in Section 5.2. The geometry consists of a central He II emission source (orange) and a partial spherical H I region (green). The central source emits UV He II lines at 1025, 972, and 949 Å. The inner radius R_i is half of the outer radius R_o . The H I scattering region is characterized by a H I column density N_{HI} .

radiation from the white dwarf, R_i is fixed at $0.5R_o$. Therefore, we consider the broad ranges of $\theta_o = 30 - 60^\circ$ and $N_{\text{HI}} = 10^{20-23} \text{ cm}^{-2}$.

To compute the RCEs of three Raman-scattered He II The UV He II photons at 1025, 972, and 949 Å are generated from the central source with the wavelength at the line center in our simulations; 10^5 photons for each line. After that, the simulations collect photons after they escape from the entire grid and estimate the ratio of Raman-scattered photons to the $n = 2$ state, which is RCEs (see Eq. 5). The detailed Monte Carlo method of STARS is described in Chang & Lee (2020).

APPENDIX B: SPATIAL DISTRIBUTION OF RAMAN-SCATTERING SITES

We investigate the spatial distribution of Raman-scattering sites associated with the three Raman-scattered He II features. Because Raman optical photons are expected to escape the neutral region immediately after scattering, the location of these events provides a direct probe of the surface brightness distribution of the Raman-scattered emission. This approach, therefore, allows us to infer how the distribution of neutral hydrogen influences the emergent Raman features. If the scattering medium is optically thin, scattering takes place throughout the entire region with almost equal probability, resulting in a uniform surface brightness. In contrast, for an optically thick scattering medium, scattering primarily occurs near the surface oriented toward the light source.

In Figure B1, we show the radial distribution of Raman photons measured from the center of the neutral region. The three panels correspond to column densities of $N_{\text{HI}} = 10^{21}$, 10^{22} , and 10^{23} cm^{-2} , shown in the top, middle, and bottom panels, respectively. In the top panel, the scattering region is optically thin for all He II transitions,

and the Raman-scattering that produces the three He II features is distributed nearly uniformly across the neutral region. In contrast, the bottom panel illustrates the optically thick case: the scattering region is opaque to Raman-scattered He II $\lambda 6545$ and $\lambda 4851$, and moderately thick for $\lambda 4332$. Consequently, the Raman photons of He II $\lambda 6545$ and $\lambda 4851$ are confined within $\sim 0.6, r/R_o$, whereas Raman He II $\lambda 4332$ originates from deeper layers around $\sim 0.8, r/R_o$.

In the middle panel, the medium is highly opaque to He II $\lambda 6545$, moderately thick to He II $\lambda 4851$, and optically thin to He II $\lambda 4332$. At a column density of $N_{\text{HI}} = 10^{22} \text{ cm}^{-2}$, these three Raman-scattered He II features therefore exhibit markedly different surface brightness distributions.

This paper has been typeset from a $\text{\TeX}/\text{\LaTeX}$ file prepared by the author.

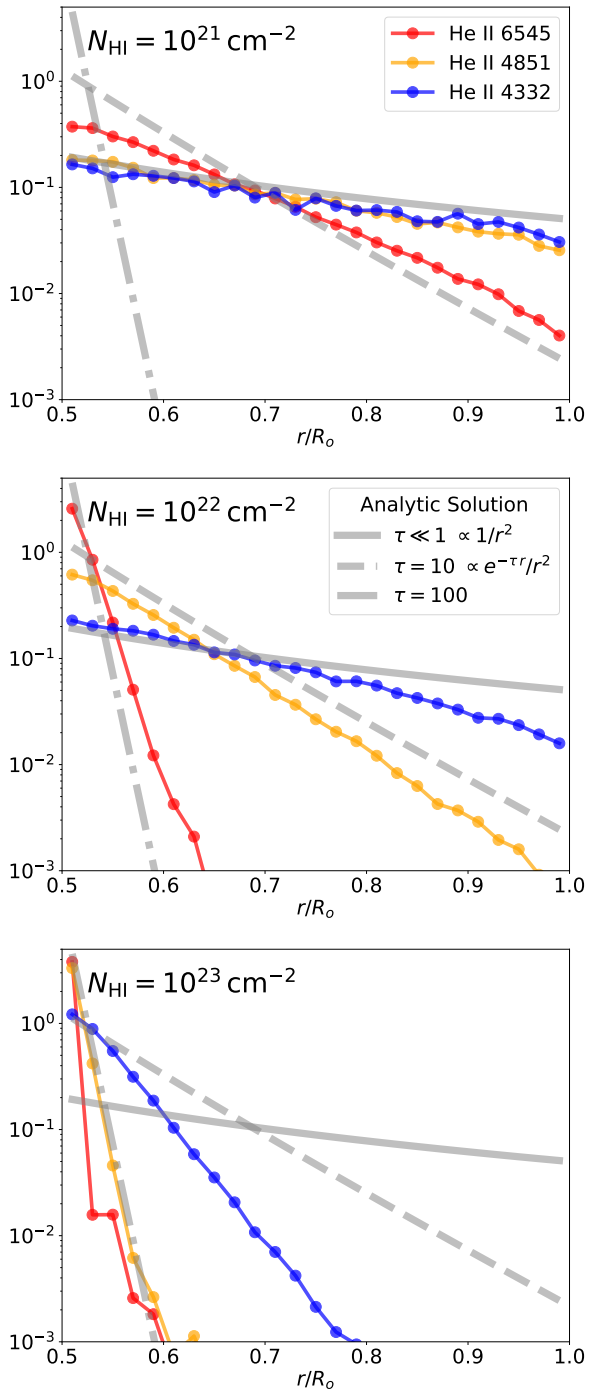


Figure B1. Histogram of the radius at the last-scattering location for different N_{HI} values of 10^{21} (top), 10^{22} (middle), and 10^{23} cm^{-2} (bottom). The red, orange, and blue lines represent Raman-scattered He II $\lambda 6545$, $\lambda 4851$, and $\lambda 4332$ features, respectively. The gray lines indicate the analytic solutions for three different optical depths: $\tau \ll 1$ (solid), $\tau = 10$ (dashed), and $\tau = 100$ (dot-dashed).